

---

# HOW (NOT) TO HYBRIDIZE NEURAL AND MECHANISTIC MODELS FOR EPIDEMIOLOGICAL FORECASTING

---

**Yiqi Su**

Department of Computer Science  
Virginia Tech  
Alexandria, USA  
yiqisu@vt.edu

**Ray Lee**

Department of Computer Science  
Virginia Tech  
Alexandria, USA  
ray.lee@vt.edu

**Jiaming Cui**

Department of Computer Science  
Virginia Tech  
Blacksburg, USA  
jiamingcui@vt.edu

**Naren Ramakrishnan**

Department of Computer Science  
Virginia Tech  
Alexandria, USA  
naren@vt.edu

February 9, 2026

## ABSTRACT

Epidemiological forecasting from surveillance data is a hard problem and hybridizing mechanistic compartmental models with neural models is a natural direction. The mechanistic structure helps keep trajectories epidemiologically plausible, while neural components can capture non-stationary, data-adaptive effects. In practice, however, many seemingly straightforward couplings fail under partial observability and continually shifting transmission dynamics driven by behavior, waning immunity, seasonality, and interventions. We catalog these failure modes and show that robust performance requires making non-stationarity explicit: we extract multi-scale structure from the observed infection series and use it as an interpretable control signal for a controlled neural ODE coupled to an epidemiological model. Concretely, we decompose infections into trend, seasonal, and residual components and use these signals to drive continuous-time latent dynamics while jointly forecasting and inferring time-varying transmission, recovery, and immunity-loss rates. Across seasonal and non-seasonal settings—including early outbreaks and multi-wave regimes—our approach reduces long-horizon RMSE by 15–35%, improves peak timing error by 1–3 weeks, and lowers peak magnitude bias by up to 30% relative strong time-series, neural ODE, and hybrid baselines, without relying on auxiliary covariates.

**Keywords** Neural ODEs · Mechanistic model · Data decomposition · Epidemiological modeling · Partial observability · Disease forecasting

## 1 Introduction

Epidemic forecasting is a central problem in public health. Given historical epidemic curves, e.g., daily infections, hospitalizations, or deaths, the goal is to predict future trajectories. Epidemiologists have developed a broad range of models that have proven effective across outbreaks such as H1N1, Ebola, and most recently, COVID-19 [11].

Most forecasting models fall into three main families: compartmental models, statistical or machine learning models, and hybrid models. Compartmental models built on ordinary differential equations (ODEs), such as SIR (Susceptible-Infectious-Recovered), SEIR, and SIRS models, have long served as the foundation of epidemiological modeling [1, 16]. However, they rely on strong assumptions about parameter stationarity [8]. Meanwhile, statistical approaches such as ARIMA, state-space models, and Gaussian processes have also been widely used, particularly for short forecasting horizons [5, 25, 12, 27]. More recently, deep learning models, including recurrent neural networks, temporal convolutional networks, and transformer-based architectures have also achieved strong empirical performance [17, 4,

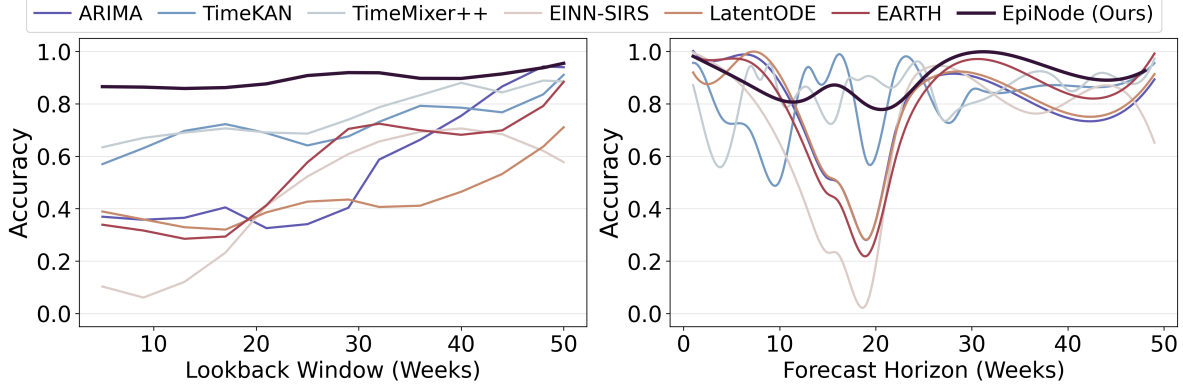


Figure 1: EpiNode accuracy as a function of lookback window and forecast horizon.

22, 37]. Yet these models typically operate as black boxes, lack epidemiological interpretability, and may produce physically inconsistent forecasts for long horizons or under regime shifts [31, 6]. To tackle this issue, hybrid frameworks that embed neural components within compartmental models have been proposed. Examples include Neural ODEs [9], latent ODEs [29], and physics-informed neural networks (PINNs). In principle, hybrid models can combine mechanistic interpretability with data-driven flexibility; in practice, however, they still face two fundamental challenges: partial observability and non-stationarity.

**Partial Observability.** Epidemiological data are inherently incomplete: typically only cases/deaths/hospitalizations (or proxies such as symptomatic rates) are observed, while other states (e.g., susceptible or exposed populations) remain latent [14, 30]. Such undetermined systems make both inference and forecasting ill-posed, since multiple latent trajectories can explain the same observations, and full-state supervision is rarely available.

**Non-Stationarity.** Key epidemiological parameters (e.g., transmission or recovery rates) evolve over time due to climate, mobility, behavior change, policy interventions, and accumulated immunity [19]. For example, influenza transmission varies across seasons and between waves, and retrospective analyses show that assuming constant parameters can induce systematic bias and degrade peak predictions [7]. Modeling time-varying parameters is therefore essential, but increases estimation complexity from  $O(n)$  to  $O(nT)$ .

Crucially, these challenges interact and amplify each other: latent states complicate parameter estimation, while parameter misestimation feeds back into incorrect latent-state reconstruction. This vicious cycle worsens with longer forecast horizons. While short-term forecasts benefit from temporal autocorrelation, accuracy deteriorates rapidly as the horizon grows: errors compound due to uncertainty in latent compartments and evolving dynamics. The effect is especially pronounced near epidemic peaks, where small growth-rate errors translate into large peak-timing and peak-magnitude errors [2]. This motivates methods that improve long-horizon stability and peak predictability and a careful accounting of when ‘hybridization’ helps versus hurts.

Our key contributions are:

- We characterize and empirically demonstrate key failure modes in neural–mechanistic hybrid epidemic models, highlighting how the wrong architecture can destabilize long-horizon rollouts and bias peak predictions.
- We propose EpiNode, a decomposition-controlled hybrid neural ODE + SIRS forecasting framework that addresses partial observability and non-stationarity by explicitly modeling the multi-scale structure of observed infection signals. This approach enforces epidemiological consistency through mechanistic SIRS equations and enables stable long-horizon rollouts when learning latent dynamics (Figure 1). Furthermore, it reconstructs time-varying parameters such as transmission, recovery, and immunity-loss rates within bounded, interpretable ranges.
- We demonstrate the universal applicability of the proposed model across seasonal and non-seasonal diseases, as well as across initial outbreaks and multi-wave historical settings, through extensive synthetic and real-world benchmarks.

## 2 Failure Modes

We begin by outlining failure modes specific to epidemiological modeling when using neural ODEs and related machine learning approaches. These modes can be viewed as ‘antipatterns’, i.e., what not to do.

### 2.1 Neural ODEs Fail under Partial Observability Even When They Fit Observed Infections.

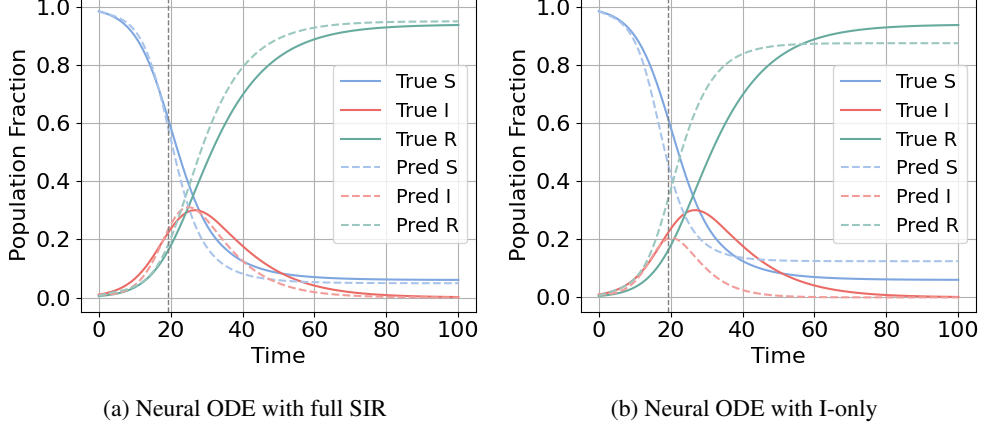


Figure 2: Failure of SIR forecasts from neural ODEs under full and partial observability at a train/forecast split of 0.2/0.8. When all compartments  $S(t), I(t), R(t)$  are observed (a), the neural ODE accurately recovers and extrapolates the epidemic dynamics. Under partial observability with only  $I(t)$  available (b), the model fits the observed infections but exhibits drift in the unobserved compartments, leading to degraded long-horizon forecasts.

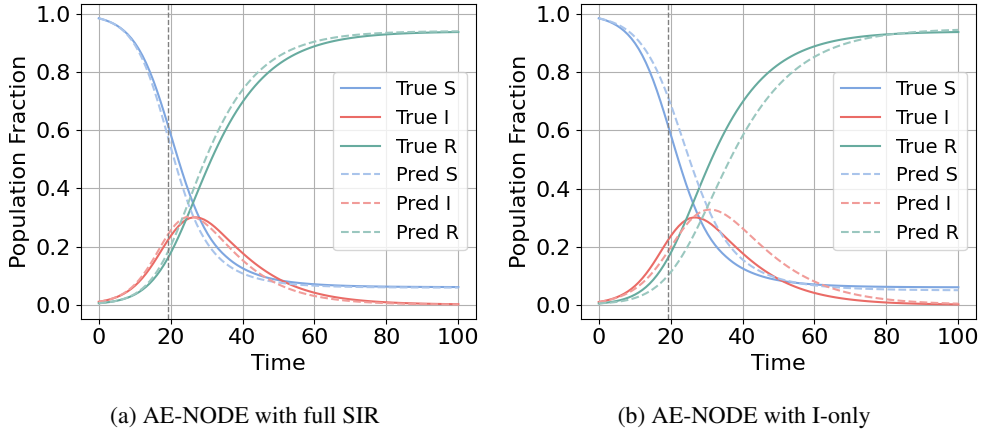
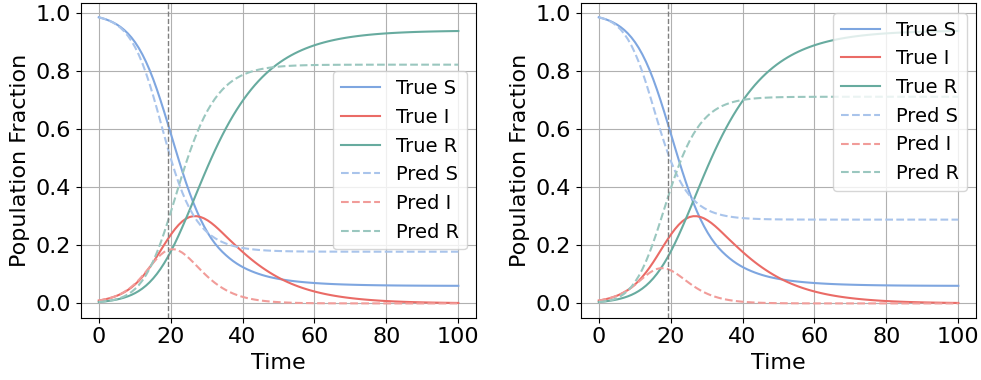


Figure 3: Failure of SIR forecasts from AE-NODE under full and partial observability at a train/forecast split of 0.2/0.8 with full-state supervision (a) and under I-only supervision (b).

We first evaluated vanilla neural ODEs [9] and autoencoder-based neural ODE (AE-NODE) pipelines, wherein an encoder mapping observations to a latent state, followed by continuous-time latent evolution, and a decoder. These models perform well when all compartments are observed (Figure 2a, Figure 3a), but their performance degrades substantially when only the infected trajectory  $I(t)$  is available (Figure 2b, Figure 3b). (This is the most reasonable assumption since infections can be assimilated from hospitalizations and other data, but other compartments are not observed.) Under partial observability, the encoder–decoder formulation introduces a non-identifiability issue: multiple latent trajectories and parameter configurations can explain the same observed  $I(t)$ . As a result, the latent dynamics can drift in unobserved dimensions while still fitting short-term observations, leading to unstable long-horizon rollouts. This highlights that latent continuous-time modeling alone is insufficient without additional structure to anchor the latent state.

## 2.2 Bidirectional (Adjoint-Based) Objectives Fail to Resolve Identifiability and Can Still Learn Implausible Latent Dynamics.



(a) AE-NODE with full SIR + bidirectional training (b) AE-NODE with I-only + bidirectional training

Figure 4: Failure of SIR forecasts from AE-NODE under short training windows, with bidirectional training.

Inspired by Koopman autoencoders [3] and adjoint sensitivity analysis in neural ODEs [9], we explored bidirectional training objectives. The adjoint formulation makes it possible to efficiently compute gradients with respect to initial conditions and model parameters by integrating an auxiliary adjoint system backward in time, effectively enabling a backward-in-time learning signal that complements forward rollout (see architecture in the Appendix; Fig A1). In principle, this backward process can regularize latent dynamics and encourage temporal consistency across the observation window.

In practice, however, while adjoint-based training improves optimization stability, it does not address the fundamental identifiability challenge under partial observability (Figure 4a). When only the infected trajectory  $I(t)$  is observed (Fig. 4b), backward gradient propagation constrains the latent dynamics to be self-consistent but does not introduce new information about unobserved compartments or time-varying drivers.

Moreover, epidemic processes are intrinsically forward-evolving, governed by causal transmission and recovery mechanisms. However, in practice, bidirectional objectives allow the model to satisfy forward and backward consistency in latent space without learning epidemiologically meaningful dynamics. This suggests that optimization refinements alone cannot compensate for missing structural cues in the input signal. As a result, the model can satisfy both forward and backward objectives while still encoding implausible latent trajectories. This highlights that adjoint-enabled bidirectional learning is a powerful optimization tool, but must be complemented with structured, forward-driving signals to reliably learn interpretable and stable epidemic dynamics.

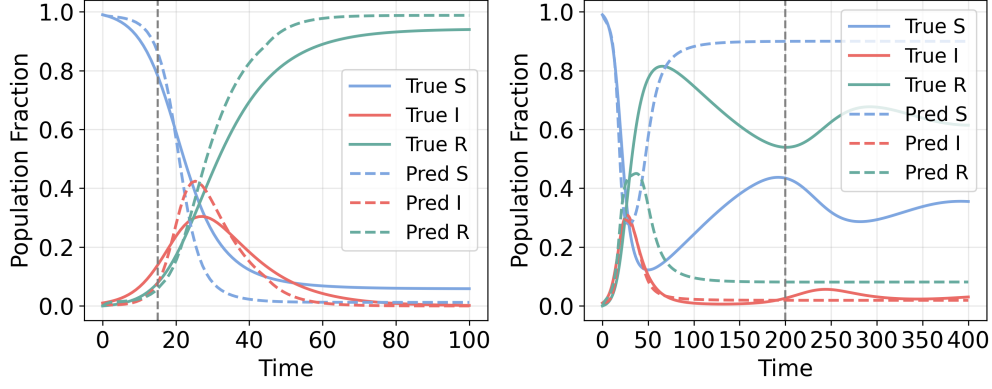
## 2.3 Physics-Informed Losses Fail under Sparse Supervision and Time-Varying Parameters by Admitting Degenerate Solutions.

We next incorporated physics-informed losses [32] that penalize violations of SIR/SIRS differential equations during training. These formulations aim to improve physical feasibility and short-term accuracy when strong prior knowledge is available.

With only  $I(t)$  observed, under the basic SIR model (Figure 5a), forecasts remain qualitatively reasonable despite partial observability. Under the more expressive SIRS model (Figure 5b), the same supervision leads to severe errors in unobserved compartments and long-horizon dynamics, highlighting a fundamental identifiability gap when recovery and reinfection processes are not directly constrained.

## 2.4 Neural CDE and CDE–ODE Hybrids Fail to Capture Multi-Wave Dynamics.

Neural Controlled Differential Equations (CDEs) [20] were evaluated as a way to incorporate the observed signal as a continuous control path. We designed a NCDE-ODE architecture (Figure A2 in the Appendix), which captures synthetic SIRS generated using time-fixed parameters effectively (Figure 6a), but struggle with SIRS and multi-wave influenza-like illness (ILI) data (Figure 6b). This limitation arises because multi-wave dynamics are driven by latent forcing processes—such as seasonality and immunity waning—that are not explicitly represented in the input channel.



(a) Physics-informed loss with I-only under SIR (b) Physics-informed loss with I-only under SIRS

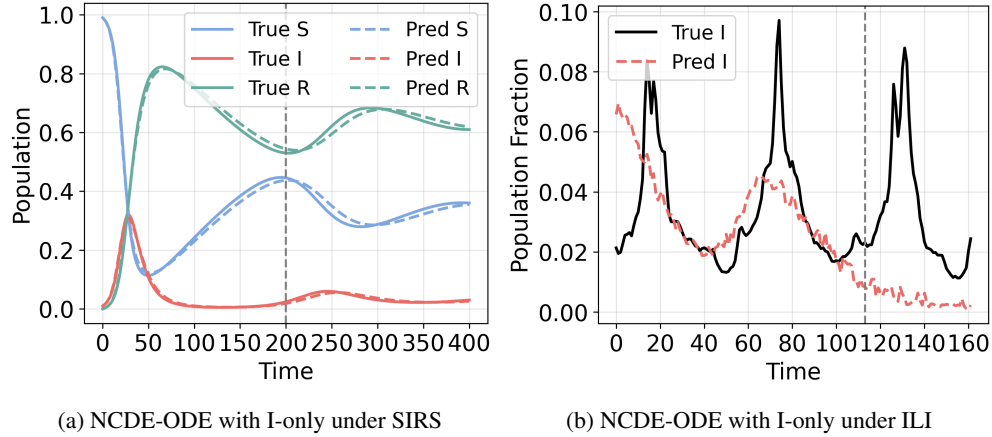
Figure 5: Incorporating physics informed losses. (a) with only  $I(t)$  observed, forecasts are reasonable with an SIR model assumption (a) but are poor under an SIRS model (b).

Figure 6: Failure of Neural CDE-ODE forecasts on real data under partial observability. Forecasts are good for SIRS model (a), but fails to capture trends for ILI data (b).

When only  $I(t)$  is provided, the model must implicitly infer these drivers, leading to poor extrapolation across epidemic waves.

### 3 EpiNode Framework

To address the above issues, we present **EpiNode** (Figure 7), a hybrid neural–physical framework for epidemic forecasting from partial observations. EpiNode integrates multi-scale signal decomposition, controlled latent continuous-time dynamics, and mechanistic SIRS evolution to jointly forecast epidemic trajectories and infer time-varying epidemiological parameters.

**Problem Setup.** Let  $\{(t_i, I_i)\}_{i=0}^{T-1}$  denote an epidemic time series, where only the infected compartment  $I(t)$  is observed at discrete times  $t_i$ . The latent epidemic state is

$$\mathbf{y}(t) = [S(t), I(t), R(t)]^\top \in \mathbb{R}_{\geq 0}^3, \quad (1)$$

with unknown, time-varying parameters  $\beta(t)$  (transmission),  $\gamma(t)$  (recovery), and  $\delta(t)$  (immunity waning). We assume  $I(0)$  is known and initialize

$$S(0) = 1 - I(0), \quad R(0) = 0. \quad (2)$$

Our objective is to forecast  $I(t)$  beyond the observation window, accurately predict epidemic peaks, and recover interpretable parameter trajectories.

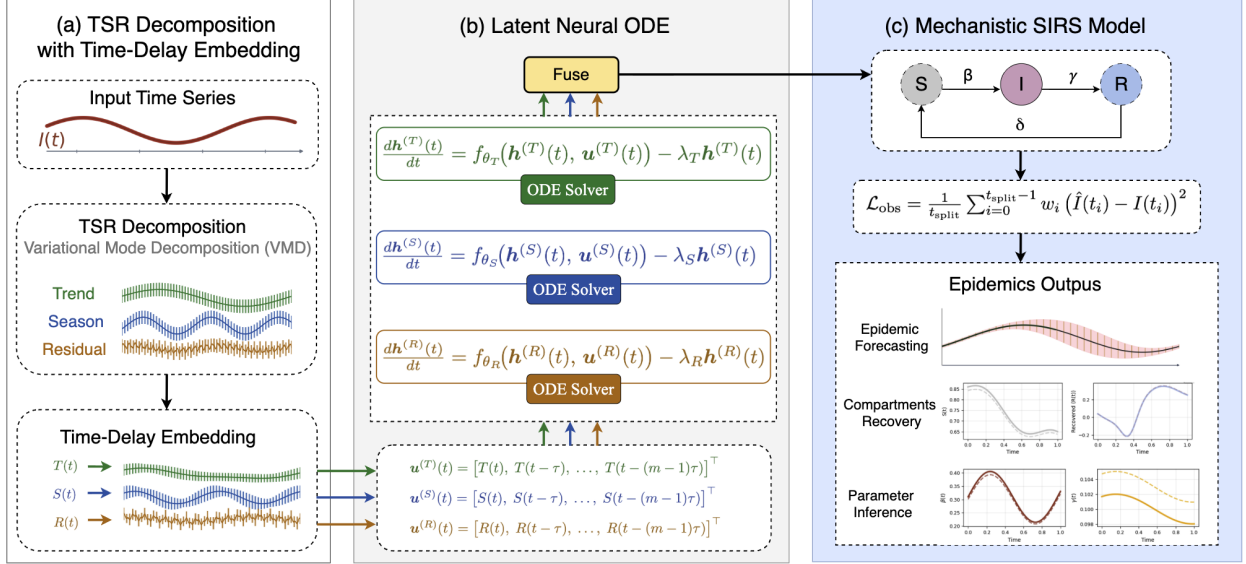


Figure 7: Overview of the proposed **EpiNode** framework. The observed epidemic time series is decomposed into *trend*, *seasonal*, and *residuals* components, which serve as multi-scale control signals for latent Neural ODEs. The fused latent representation is decoded into time-varying epidemiological parameters and coupled with mechanistic SIRS dynamics to produce physically consistent forecasts and interpretable parameter trajectories.

**Variational Mode Decomposition (VMD).** Given a real-valued epidemic signal  $x(t)$ , we use Variational Mode Decomposition (VMD) [13] to decompose it into  $K$  intrinsic mode functions  $\{u_k(t)\}_{k=1}^K$ , each associated with a center frequency  $\omega_k$ , by minimizing the total bandwidth of the modes subject to exact signal reconstruction. The constrained variational problem is defined as

$$\begin{aligned} \min_{\{u_k\}, \{\omega_k\}} \quad & \sum_{k=1}^K \left\| \partial_t \left[ \left( \delta(t) + \frac{j}{\pi t} \right) * u_k(t) \right] e^{-j\omega_k t} \right\|_2^2 \\ \text{s.t.} \quad & \sum_{k=1}^K u_k(t) = x(t), \end{aligned} \quad (3)$$

where  $(\delta(t) + \frac{j}{\pi t}) * u_k(t)$  denotes the analytic signal of  $u_k(t)$  obtained via the Hilbert transform,  $\partial_t$  is the temporal derivative, and  $*$  denotes convolution. This objective encourages each mode to be compact around its center frequency while collectively reconstructing the original signal.

**Augmented Lagrangian Formulation.** The constrained problem in (3) is solved using the alternating direction method of multipliers (ADMM) by forming the augmented Lagrangian

$$\begin{aligned} \mathcal{L}(\{u_k\}, \{\omega_k\}, \lambda) = \alpha \sum_{k=1}^K \left\| \partial_t \left( \left( \delta(t) + \frac{j}{\pi t} \right) * u_k(t) \right) e^{-j\omega_k t} \right\|_2^2 \\ + \left\| x(t) - \sum_{k=1}^K u_k(t) \right\|_2^2 \\ + \left\langle \lambda(t), x(t) - \sum_{k=1}^K u_k(t) \right\rangle. \end{aligned} \quad (4)$$

where  $\lambda(t)$  is the Lagrange multiplier and  $\alpha > 0$  controls the bandwidth penalty.

**ADMM Updates.** Let  $\hat{x}(\omega)$ ,  $\hat{u}_k(\omega)$ , and  $\hat{\lambda}(\omega)$  denote the Fourier transforms of  $x(t)$ ,  $u_k(t)$ , and  $\lambda(t)$ , respectively. The ADMM updates admit closed-form solutions in the frequency domain. At iteration  $n + 1$ , the mode update is

$$\hat{u}_k^{n+1}(\omega) = \frac{\hat{x}(\omega) - \sum_{i \neq k} \hat{u}_i^n(\omega) + \frac{1}{2} \hat{\lambda}^n(\omega)}{1 + 2\alpha (\omega - \omega_k^n)^2}, \quad (5)$$

and the center frequency is updated as the energy-weighted mean frequency

$$\omega_k^{n+1} = \frac{\int_0^\infty \omega |\hat{u}_k^{n+1}(\omega)|^2 d\omega}{\int_0^\infty |\hat{u}_k^{n+1}(\omega)|^2 d\omega}. \quad (6)$$

The Lagrange multiplier is updated by

$$\hat{\lambda}^{n+1}(\omega) = \hat{\lambda}^n(\omega) + \tau \left( \hat{x}(\omega) - \sum_{k=1}^K \hat{u}_k^{n+1}(\omega) \right), \quad (7)$$

where  $\tau > 0$  is the dual ascent step size. Iterations continue until convergence. VMD produces an ensemble of band-limited modes with distinct frequency characteristics. In our framework, these modes are grouped into trend, seasonal, and residuals (high-frequency components) and used as structured forcing signals for downstream epidemic modeling:

$$I(t) = T(t) + S(t) + N(t), \quad (8)$$

where  $T(t)$  captures low-frequency trends,  $S(t)$  captures periodic or seasonal structure, and  $N(t)$  represents residual fluctuations. This decomposition isolates distinct temporal scales that would otherwise be confounded in a single observation stream.

**Time-Delay Embedding of Control Signals.** To provide temporal context and improve identifiability, we optionally apply a time-delay embedding independently to each component. For a component  $x(t) \in \{T(t), S(t), R(t)\}$ , corresponding to trend, seasonality, and residual respectively, we construct the lag-augmented control

$$\mathbf{u}^{(x)}(t) = [x(t), x(t - \tau), \dots, x(t - (m - 1)\tau)]^\top \in \mathbb{R}^m, \quad (9)$$

where  $\tau$  is the delay and  $m$  is the embedding dimension. Each delay-embedded control  $\mathbf{u}^{(x)}(t)$  is then provided to its own latent Neural ODE, allowing the model to capture component-specific temporal dependencies before fusion. When delay embedding is disabled, the control reduces to the instantaneous signal, i.e.,  $\mathbf{u}^{(x)}(t) = x(t)$ .

**Collaborated Latent Neural ODEs.** We maintain three latent states corresponding to the TSR components:

$$\mathbf{h}^{(T)}(t) \in \mathbb{R}^{d_T}, \quad \mathbf{h}^{(S)}(t) \in \mathbb{R}^{d_S}, \quad \mathbf{h}^{(R)}(t) \in \mathbb{R}^{d_R}. \quad (10)$$

Each latent state evolves according to a Neural ODE:

$$\frac{d\mathbf{h}^{(c)}(t)}{dt} = f_{\theta_c}(\mathbf{h}^{(c)}(t), \mathbf{u}^{(c)}(t)) - \lambda_c \mathbf{h}^{(c)}(t), \quad (11)$$

where  $f_{\theta_c}$  is a neural vector field,  $c \in \{T, S, R\}$ ,  $\mathbf{u}^{(c)}(t)$  is the TSR-based control input from (9), and  $\lambda_c \geq 0$  is a learnable damping coefficient implemented via softplus( $\cdot$ ). The ODEs are numerically integrated between observation times using an explicit solver (RK4 in our experiments).

**Latent Fusion and Parameter Decoding.** The latent states are fused into a shared representation:

$$\mathbf{h}(t) = \text{Fuse}([\mathbf{h}^{(T)}(t); \mathbf{h}^{(S)}(t); \mathbf{h}^{(R)}(t)]), \quad (12)$$

where  $\text{Fuse}(\cdot)$  is a multilayer perceptron. From  $\mathbf{h}(t)$ , we decode epidemiological parameters using a bounded parameter network:

$$(\tilde{\beta}(t), \tilde{\gamma}(t), \tilde{\delta}(t)) = g_\phi(\mathbf{h}(t)), \quad \tilde{\cdot} \in (0, 1), \quad (13)$$

followed by affine scaling into disease-specific ranges:

$$\begin{aligned} \beta(t) &= \beta_{\min} + (\beta_{\max} - \beta_{\min})\tilde{\beta}(t), \\ \gamma(t) &= \gamma_{\min} + (\gamma_{\max} - \gamma_{\min})\tilde{\gamma}(t), \\ \delta(t) &= \delta_{\min} + (\delta_{\max} - \delta_{\min})\tilde{\delta}(t). \end{aligned} \quad (14)$$

**Evolving Epidemic Trajectories.** Given the decoded parameters, the epidemic state evolves according to the SIRS equations:

$$\begin{aligned}\dot{S}(t) &= -\beta(t) S(t) I(t) + \delta(t) R(t), \\ \dot{I}(t) &= \beta(t) S(t) I(t) - \gamma(t) I(t), \\ \dot{R}(t) &= \gamma(t) I(t) - \delta(t) R(t).\end{aligned}\tag{15}$$

We integrate (15) using an RK4 step with  $\Delta t_i = t_{i+1} - t_i$ . After each step, we enforce non-negativity and approximate mass conservation:

$$\mathbf{y}(t_{i+1}) \leftarrow \alpha \frac{\mathbf{y}(t_{i+1})}{\|\mathbf{y}(t_{i+1})\|_1} + (1 - \alpha) \mathbf{y}(t_i),\tag{16}$$

with  $\alpha = 0.9$  in all experiments. The predicted infection trajectory is  $\hat{I}(t) = (\mathbf{y}(t))_2$ .

**Training objective.** Let  $t_{\text{split}}$  denote the end of the observation window. We train EpiNode end-to-end by minimizing a weighted mean squared error on the infected compartment:

$$\mathcal{L}_{\text{obs}} = \frac{1}{t_{\text{split}}} \sum_{i=0}^{t_{\text{split}}-1} w_i (\hat{I}(t_i) - I(t_i))^2,\tag{17}$$

where  $w_i$  increases linearly near the end of the training window to emphasize alignment at the forecast boundary. Gradients are backpropagated through all components, including the ODE solvers.

## 4 Experimental Results

Our experiments are intended to answer the below questions:

1. **Performance Evaluation (Section 4.5)**
  - (a) **Forecasting Accuracy.** How accurately does the model predict the full infection trajectory over time? (Section 4.5.1)
  - (b) **Peak Errors.** How accurately does the model predict the magnitude and timing of the infection peak? (Section Appendix 4.5.2)
2. **Applications (Section 4.6)**
  - (a) **Inference of Time-Varying Parameters.** Is the model able to recover meaningful and smooth trajectories of time-dependent epidemiological parameters? (Section 4.6.1)
  - (b) **Regional Dynamics.** Is EpiNode able to capture regional dynamics of infectious disease transmission? (Section 4.6.2)
3. **Ablation Analysis (Section 4.7)**
  - (a) **Decomposition vs Non-Decomposition.** Does decomposing the observed infection time series improve modeling and forecasting performance compared to using the raw signal directly? (Section 4.7.1)
  - (b) **Effect of Decomposition Order.** How does the number of decomposed components affect performance? (Section 4.7.2)
  - (c) **Decomposition Methods.** How do different decomposition choices affect model accuracy? (Section 4.7.3)
  - (d) **Contribution of Time Delay.** How does applying a time delay to the decomposed components influence prediction accuracy and learned dynamics? (Section 4.7.4)

### 4.1 Benchmarking Models

We compare against a diverse set of baselines, including (1) classical statistical and nonlinear sequence baselines (ARIMA, RNN-based models (LSTM)), (2) state-of-the-art univariate forecasters that leverage decomposition or multiscale mixing to capture long-range temporal patterns (TimeKAN [18] and TimeMixer++ [35]), (3) a physics-informed neural model (EINN [28]), (4) ODE-based continuous-time models (Neural ODE [9], Latent ODE [29], and KAN-ODE [21]) (5) a graph-based neural ODE model (EARTH [34]) (see details in Appendix C). Specifically, as EINN employs SEIRm physics, we adapt the framework in two ways: a) replace SEIRm with SIRS, b) predict I rather than m. In both options, I is the only observed compartment. Besides, Since we are focused on single region forecasting,

we treat the single region as a graph with  $N = 1$  node and set adjacency  $A = [1]$  in EARTH. All models are evaluated under a *single-variate input* setting.

Table 1 summarizes the modeling capabilities of representative baselines and highlights the gaps that motivate our design.

Table 1: Comparison of modeling capabilities across baselines. “TV Params” indicates inference of time-varying parameters. † EARTH is designed for multi-region graph forecasting; the univariate case reduces to a degenerate one-node graph without spatial coupling.

Model	Univariate	Cont.-time	Physics	TV Params	Interpretable	Non-seasonality	Seasonality	Stable	Long-horizon
ARIMA	✓	✗	✗	✗	✗	✗	✗	✗	✗
RNN (LSTM)	✓	✗	✗	✗	✗	✗	✗	✗	✗
TimeKAN	✓	✗	✗	✗	✗	✗	✓	✗	✗
TimeMixer++	✓	✗	✗	✗	✗	✗	✓	✗	✗
EINN	✓	✗	✓	✗	✓	✗	✗	✗	✗
Neural ODE	✓	✓	✗	✗	✗	✗	✗	✗	✗
Latent ODE	✓	✓	✗	✗	✗	✗	✗	✗	✗
KAN-ODE	✓	✓	✗	✗	✗	✗	✗	✗	✗
EARTH	†	✓	✓	✓	✓	✓	✓	✓	✓
EpiNode (ours)	✓	✓	✓	✓	✓	✓	✓	✓	✓

## 4.2 Ablation Procedures

**Single Latent ODE.** We replace the three collaborated Neural ODEs in (11) with a single latent state  $\mathbf{z}(t)$  as

$$\frac{d\mathbf{z}(t)}{dt} = f_\theta(\mathbf{z}(t), [\mathbf{u}^{(T)}(t); \mathbf{u}^{(S)}(t); \mathbf{u}^{(R)}(t)]) - \lambda \mathbf{z}(t), \quad (18)$$

followed by the same fusion, parameter decoding, and SIRS rollout. This variant isolates the benefit of disentangling multi-scale dynamics into separate latent flows.

**Number of Decomposed Signals.** To study the impact of the number of decomposition components, we compare the accuracy over 1-component (1C) vs 2C vs 3C. In the case of 1C, the input time-series data will not be decomposed and thus this reverts to a vanilla neural ODE.

**Choice of Decomposition Methods.** We further examine which decomposition methods are most effective at producing band-limited components with well-separated frequency content. The decomposition techniques evaluated include MA (moving average [36]), STL (Seasonal–Trend decomposition using Loess [24]), VMD, Wavelet [23], SSA–VMD [15], and Neural Koopman–based approaches [33], covering a broad range of design philosophies (see details in Appendix D).

**Time Delay.** When delay embedding is disabled,  $\mathbf{u}^{(x)}(t) = x(t)$ .

## 4.3 Datasets

### 4.3.1 Synthetic Datasets

**SIRS with time-fixed and time-varying parameters.** We generate synthetic epidemics using the SIRS model under multiple parameter regimes: (1) in the fixed setting (SIRS (Fixed)), transmission ( $\beta$ ), recovery ( $gamma$ ), and immunity-loss ( $\delta$ ) rates remain constant over time, serving as a baseline for identifiability under stationarity; in the time-varying setting (SIRS (Varying)), parameters evolve periodically to emulate seasonal forcing, capturing recurring epidemic patterns.

**Mismatched Epidemic Physics.** To assess robustness to physics mismatch, we simulate data from alternative compartmental models: (1) the SIR setting removes immunity waning, testing the model’s ability to adapt when the assumed SIRS structure is over-parameterized; (2) the SEIRS setting introduces an exposed compartment, increasing latent-state complexity and evaluating performance when the true dynamics deviate from the assumed model class.

### 4.3.2 Real-World Datasets

**Seasonal Epidemics.** We use weekly Influenza-like illness (ILI) surveillance data collected by the U.S. Centers for Disease Control and Prevention (CDC) (available at <https://gis.cdc.gov/grasp/fluview/fluportaldashboard.html>) from all 10 U.S. Department of Health and Human Services (HHS) regions over a three-year period (Week 30, 2022–Week 30, 2025).

**Non-Seasonal Epidemics.** We evaluate on a non-seasonal dataset of the 7-day averaged U.S. COVID-like illness symptoms (CLS) provided by Delphi/COVIDcast (<https://delphi.cmu.edu/covidcast/survey-results/?date=20220625>), focusing on the first wave (July 1, 2021–November 1, 2021).

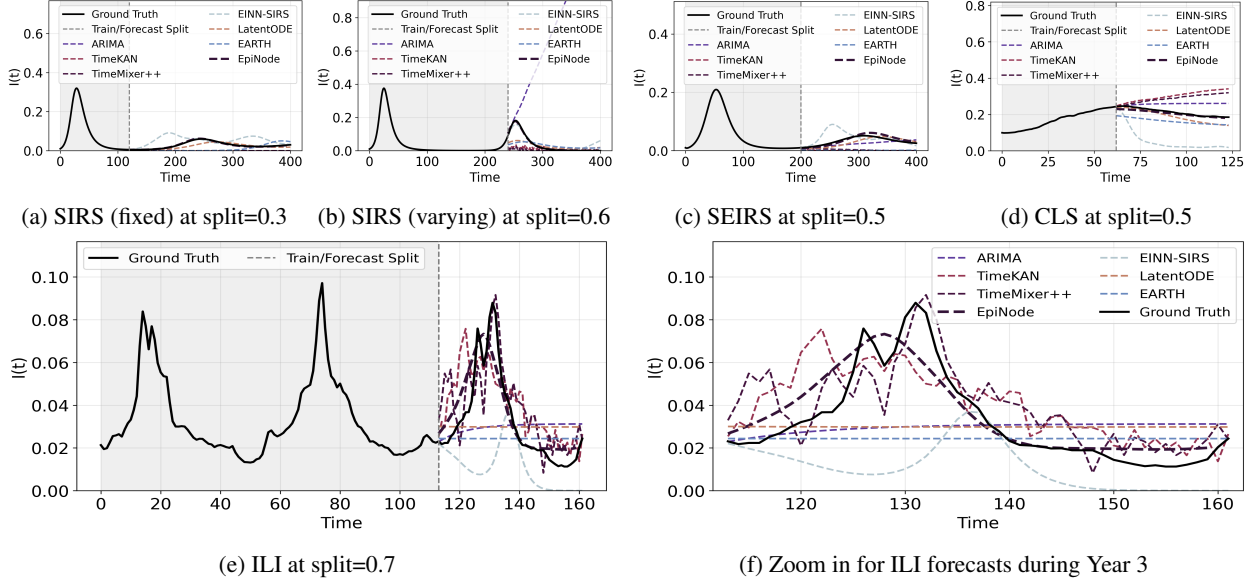


Figure 8: Comparison of forecasts on synthetic and real datasets.

### 4.4 Evaluation Protocol

We evaluate all models under a unified protocol: **(1) Forecast accuracy:** evaluate forecasting performance using standard pointwise error metrics on the infection trajectory. **(2) Peak detection accuracy:** evaluate peak detection performance by comparing the *predicted and true peak values* (magnitude) and the *predicted and true peak times* (timing). For multi-wave sequences, we focus on the dominant peak within the forecasting window. **(3) Parameter estimation:** for models that infer epidemiological parameters, evaluate the quality of the *estimated parameter trajectories*.

**Evaluation Metrics.** Across all experiments, we report standard error metrics, including RMSE and MAE. All results are averaged over multiple random seeds to ensure statistical robustness.

### 4.5 Performance Evaluation

#### 4.5.1 Forecasting Accuracy

Figure 8 compares forecast trajectories across synthetic and real datasets under representative Train/Forecast Splits. On synthetic SIRS data with fixed parameters (Figure 8a), most models achieve reasonable short-term accuracy; however, EpiNODE is the only method that consistently maintains stable long-horizon rollouts without drift in unobserved compartments. In the time-varying SIRS setting (Figure 8b), which introduces periodic forcing and immunity waning, the gap between EpiNODE and baselines widens. Pure Neural ODE, Latent ODE, and KAN-ODE struggle to extrapolate across multiple waves, while physics-informed EINN exhibits biased peak magnitudes due to limited flexibility in handling nonstationary parameters. On physics-mismatched settings (SEIRS (Figure 8c) and SIR (Figure 9c)), EpiNODE remains stable despite under- or over-parameterization of the assumed SIRS model.

For real-world datasets (non-seasonal CLS and seasonal ILI), Figure 8d and Figure 8e (Figure 8f) shows that EpiNODE consistently outperforms strong univariate baselines (TimeKAN, TimeMixer++) and continuous-time models in long-

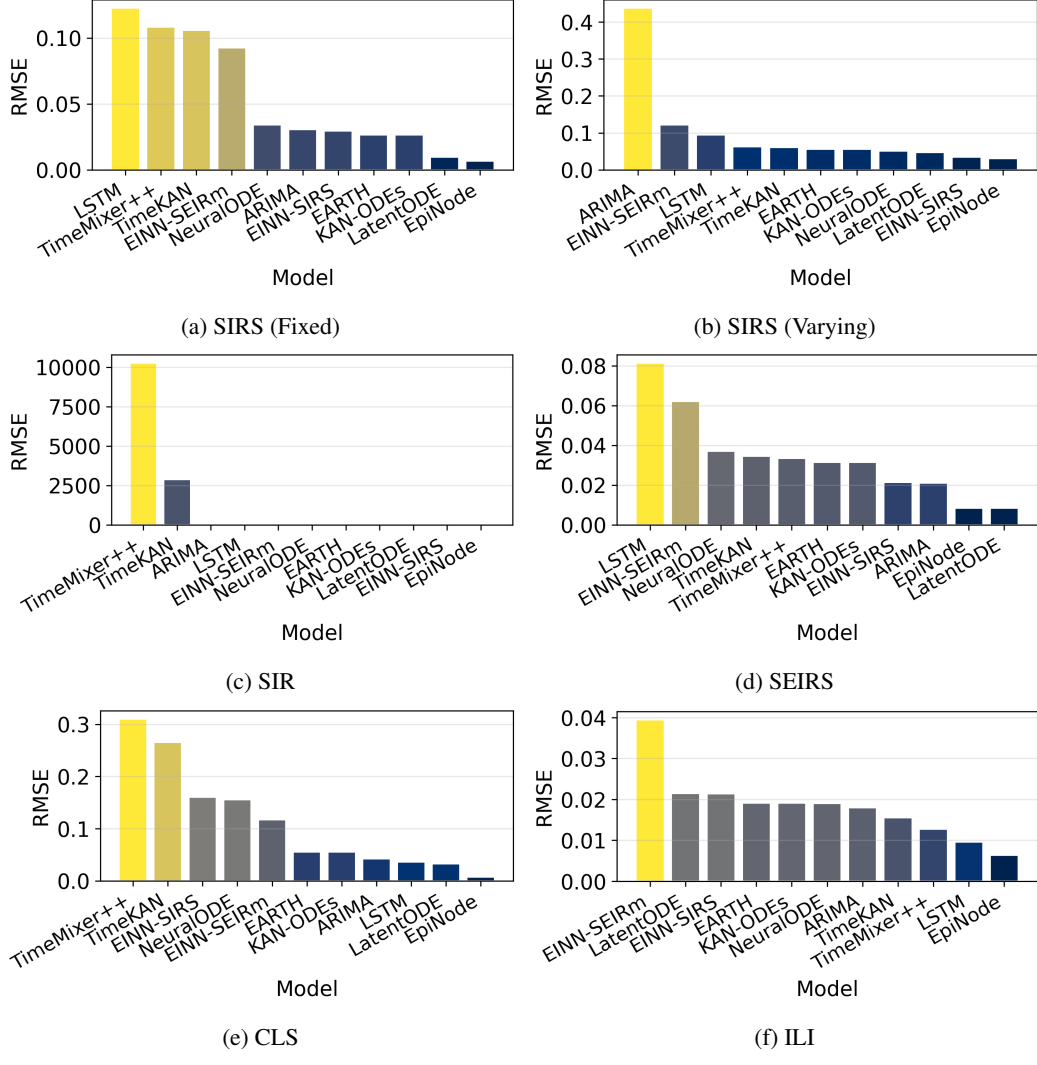


Figure 9: Overall benchmark RMSE on real datasets.

horizon accuracy. Figure 9 shows the overall RMSE across both synthetic and real datasets. EpiNode achieves lowest values on all datasets, demonstrating robustness to structured nonstationarity.

#### 4.5.2 Peak Detection

Figure 10 summarizes peak time and peak value errors across datasets. While many baselines achieve low pointwise RMSE, they often exhibit systematic bias in peak timing—either predicting peaks too early (over-aggressive growth) or too late (excessive damping).

EpiNODE consistently yields lower peak timing error and reduced bias in peak magnitude, particularly in multi-wave and seasonal settings. This improvement stems from explicitly modeling slow trend and seasonal forcing via TSR decomposition, which stabilizes the inferred growth rate near turning points. Baselines that rely solely on latent dynamics or static parameters tend to accumulate small growth-rate errors that amplify near peaks.

### 4.6 Applications

#### 4.6.1 Parameter Inference

On synthetic data (Figures 11, A4, A5), where ground truth for both unobserved compartments and time-varying parameters is available, the model accurately recovers not only the transmission rates but also the latent compartment

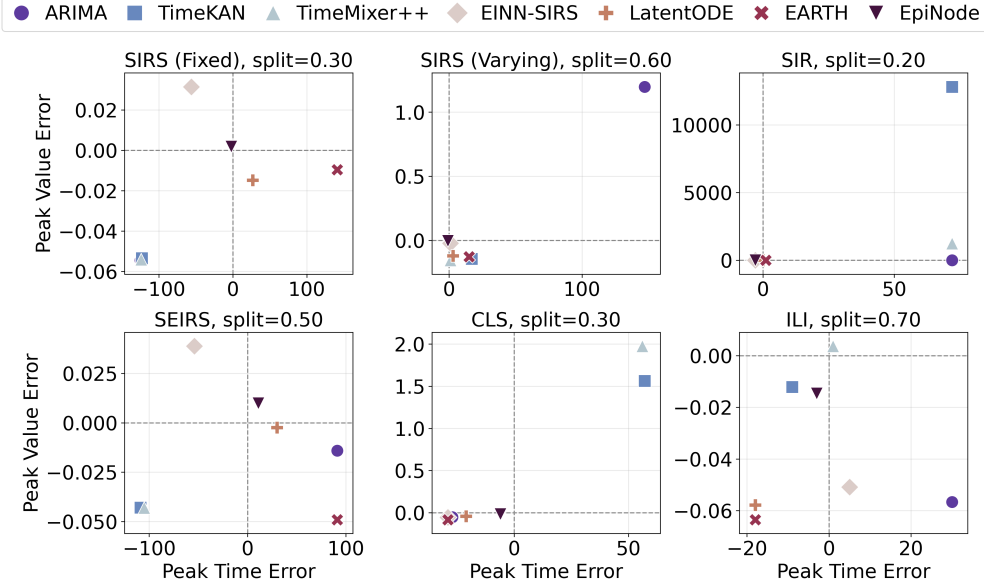


Figure 10: Peak error (magnitude &amp; timing) across datasets

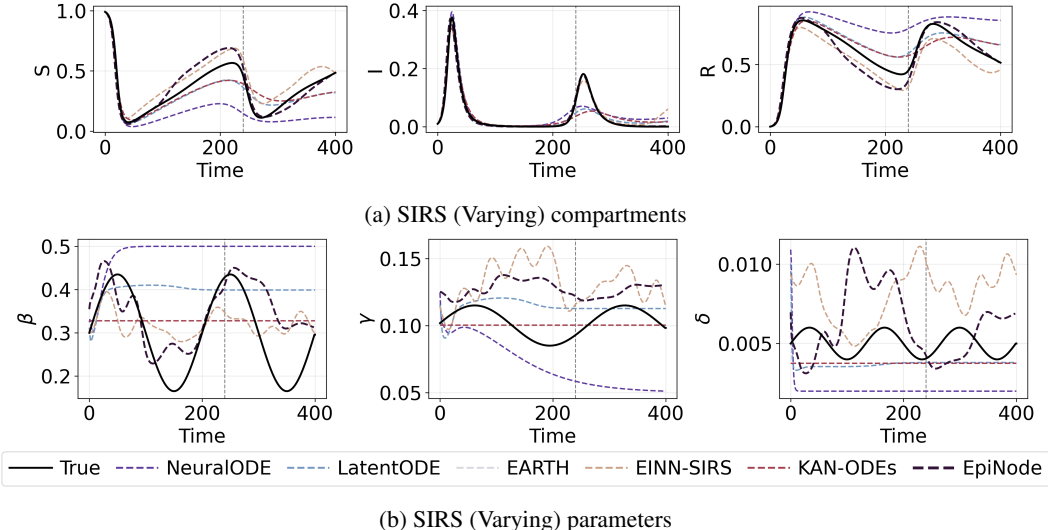


Figure 11: Unobserved compartments (a) and parameters (b) inferred from the full observation window.

trajectories. In particular, the inferred susceptible and recovered populations closely follow the true  $S(t)$  and  $R(t)$  dynamics, while the estimated rate functions  $\beta(t)$ ,  $\gamma(t)$ , and  $\delta(t)$  closely track their ground-truth counterparts. This demonstrates that EpiNode can reliably reconstruct the full epidemic state and underlying dynamical parameters under partial observability, even when only infection counts are observed. Figure 12 shows inferred epidemiological parameters using the full observation window. For a representative region (HHS 4, Figure 12a), the estimated  $\beta(t)$  exhibits clear seasonal oscillations aligned with major ILI waves, while  $\gamma(t)$  remains relatively stable and  $\delta(t)$  varies smoothly with lower amplitude. Aggregated results across all HHS regions (Figure 12b) reveal consistent seasonal modulation in  $\beta(t)$  with moderate regional heterogeneity, indicating shared seasonal forcing with region-specific transmission intensity. Importantly, inferred parameters remain smooth, bounded, and temporally coherent across regions, demonstrating stable and interpretable latent parameter recovery from real-world surveillance data under partial observability.

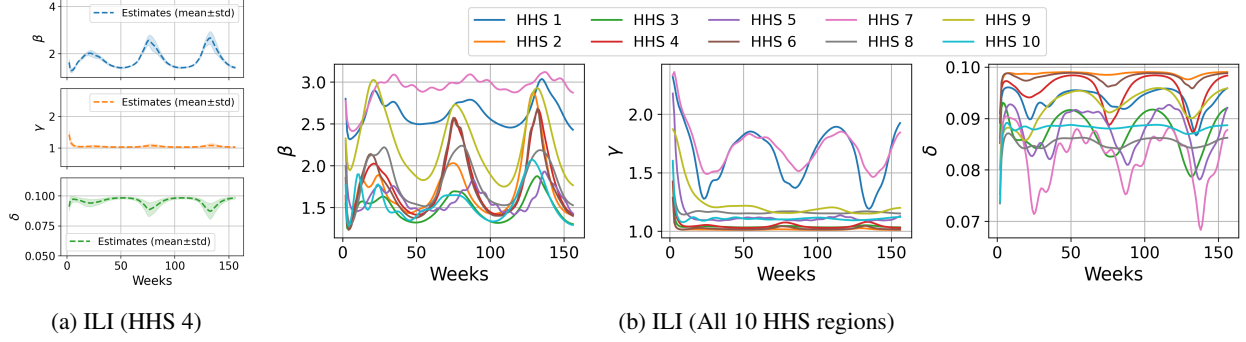


Figure 12: Inferred time-varying epidemiological parameters using the full observation window. (a) Estimated parameter rates for a representative HHS region (HHS 4). (b) Aggregated parameter estimates across all ten HHS regions.

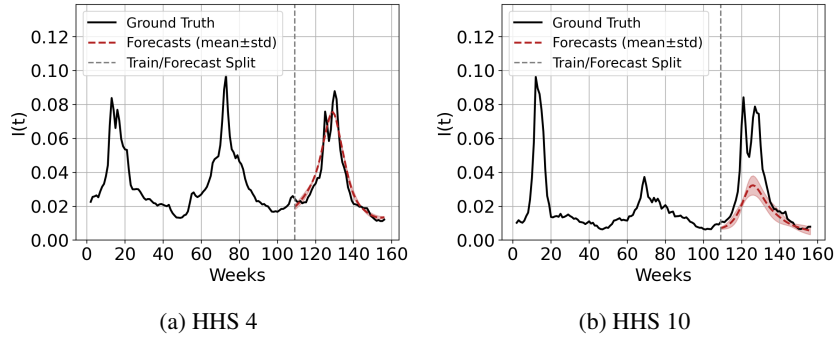


Figure 13: Best (HHS 4) and worst (HHS 10) forecasts across HHS regions at split 0.7.

#### 4.6.2 Structured Regional Dynamics Enable Accurate Forecasting

Figure 13 compares representative best and worst forecasts across HHS regions at a 0.7 train-forecast split. Figure A6 shows the forecasts across all ten HHS regions. In HHS 4 and HHS 8, the proposed model accurately captures both the timing and magnitude of the post-split infection peak, reflecting the presence of regular seasonal structure and smoothly varying trends that are well separated by the TSR decomposition. In contrast, forecasts in HHS 7 and HHS 10 are less accurate, particularly around the post-split surge. These regions exhibit more irregular dynamics and abrupt changes in peak amplitude that are weakly represented in the training window, leading to larger residual components and a pronounced distribution shift at forecast time. As a result, the inferred transmission dynamics underestimate the rapid increase, yielding peak under-prediction. These results highlight that forecast accuracy depends strongly on the structural regularity of regional epidemic dynamics.

#### 4.7 Ablation Studies

We conduct extensive ablations to isolate the contribution of key architectural components.

##### 4.7.1 Single Latent ODE Variant

Figure 14a compares architectures with a single latent ODE (1ODE) versus three collaborated latent ODEs (3ODEs) corresponding to trend, seasonal, and residual components. Under identical training conditions, 3ODEs consistently achieves lower error than 1ODE variants, particularly when time-delay embedding is enabled. This indicates that disentangling multi-scale dynamics into separate latent flows improves identifiability and long-horizon stability.

##### 4.7.2 Number of Decomposed Components

Figure 14b shows the comparison among 1 component (C) vs 2C vs 3C. Across all datasets, RMSE decreases with one to two to three components, suggesting that three components provide the most effective signals to separate slow structural evolution from seasonal forcing.

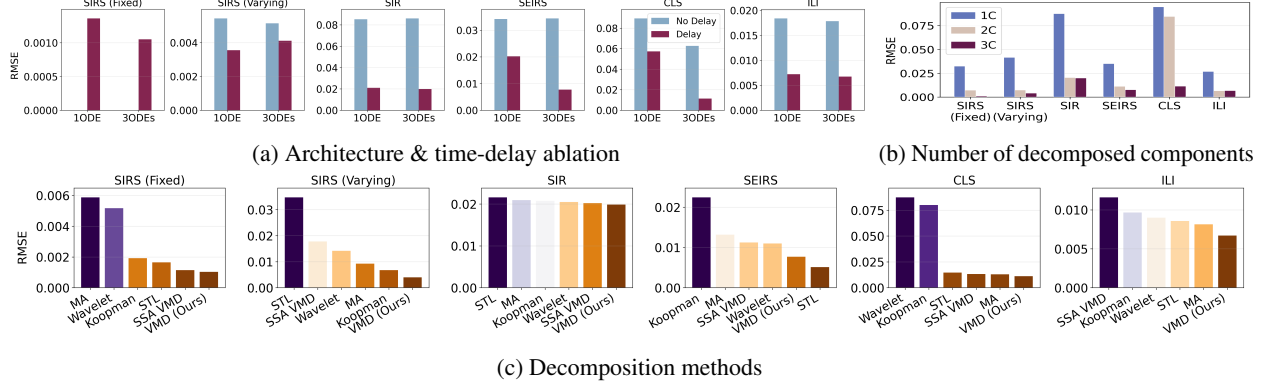


Figure 14: Ablation results across datasets. (a) Comparison of 1ODE vs. 3ODEs with and without time-delay embedding. (b) Comparison of 1-component *vs* 2-components *vs* 3-component decomposition. (c) Comparison of signal decomposition methods.

#### 4.7.3 TSR Decomposition Method

Figure 14c shows that VMD-based decomposition ranks best for almost all datasets and the second for SEIRS model, likely due to its explicit frequency localization and robustness to noise.

#### 4.7.4 Time-Delay Embedding

Incorporating time-delay embedding further improves accuracy by providing temporal context to each component (Figure 14a). An exception occurs in the SIRS setting with time-fixed parameters, where the dynamics are noise-free and stationary; in this case, time-delay embedding offers little benefit, as the system evolution is determined by the current state.

## 5 Conclusion

This work highlights the importance of integrating multi-scale structure, continuous-time latent dynamics, and mechanistic constraints for epidemic forecasting under partial observability. By explicitly decomposing the observed signal into trend, seasonal, and residuals components, EpiNode separates these effects into structured, low-dimensional control signals that guide the latent neural ODE. Our experimental results demonstrate that EpiNode produces interpretable time-varying parameter trajectories and generates forecasts consistent with known epidemiological behavior, such as seasonal and temporal variation in transmission rates. These parameter estimates provide insights beyond point forecasts, enabling retrospective analysis and hypothesis generation about underlying drivers of epidemic dynamics.

Despite these advantages, EpiNode has limitations. The current formulation focuses on single-region, deterministic dynamics and does not explicitly model uncertainty, spatial coupling, or intervention effects. Incorporating modules for such effects either as updates to the dynamics or as learnable decomposition modules represent promising directions for future work.

## Software and Data

We release the full implementation at <https://anonymous.4open.science/r/EPI-NODE/>.

## References

- [1] Roy M. Anderson and Robert M. May. *Infectious Diseases of Humans: Dynamics and Control*. Oxford University Press, 1992.
- [2] Nino Antulov-Fantulin and Lucas Böttcher. “On the accuracy of short-term COVID-19 fatality forecasts”. In: *BMC Infectious Diseases* 22.1 (Mar. 2022), p. 251. DOI: 10.1186/s12879-022-07205-9.
- [3] Omri Azencot et al. “Forecasting sequential data using consistent Koopman autoencoders”. In: *Proceedings of the 37th International Conference on Machine Learning*. ICML’20. JMLR.org, 2020.
- [4] Shaojie Bai, J. Zico Kolter, and Vladlen Koltun. “An empirical evaluation of generic convolutional and recurrent networks for sequence modeling”. In: *arXiv preprint arXiv:1803.01271* (2018).
- [5] George E. P. Box, Gwilym M. Jenkins, and Gregory C. Reinsel. *Time Series Analysis: Forecasting and Control*. Wiley, 2015.
- [6] Johannes Bracher et al. “Evaluating epidemic forecasts in an interval format”. In: *PLoS Computational Biology* 17.2 (2021), e1008618.
- [7] Elisabet Castro Blanco et al. “A Predictive Model of the Start of Annual Influenza Epidemics”. In: *Microorganisms* 12.7 (2024). ISSN: 2076-2607. DOI: 10.3390/microorganisms12071257. URL: <https://www.mdpi.com/2076-2607/12/7/1257>.
- [8] Simon Cauchemez and Neil M. Ferguson. “Realistic distributions of infectious periods in epidemic models”. In: *Proceedings of the Royal Society B* 273.1596 (2006), pp. 2491–2499.
- [9] Ricky T. Q. Chen et al. “Neural Ordinary Differential Equations”. In: *Advances in Neural Information Processing Systems*. Ed. by S. Bengio et al. Vol. 31. Curran Associates, Inc., 2018. URL: [https://proceedings.neurips.cc/paper\\_files/paper/2018/file/69386f6bb1dfed68692a24c8686939b9-Paper.pdf](https://proceedings.neurips.cc/paper_files/paper/2018/file/69386f6bb1dfed68692a24c8686939b9-Paper.pdf).
- [10] Tian Qi Chen et al. “Neural ordinary differential equations”. In: *NeurIPS* (2018).
- [11] Anne Cori and Adam Kucharski. “Inference of epidemic dynamics in the COVID-19 era and beyond”. In: *Epidemics* 48 (2024), p. 100784. ISSN: 1755-4365. DOI: <https://doi.org/10.1016/j.epidem.2024.100784>. URL: <https://www.sciencedirect.com/science/article/pii/S1755436524000458>.
- [12] Anne Cori, Britta Lassmann, and Pierre Nouvellet. “Data needs for better surveillance and response to infectious disease threats”. In: *Epidemics* 43 (June 2023). Editorial, p. 100685. ISSN: 1755-4365. DOI: 10.1016/j.epidem.2023.100685.
- [13] Konstantin Dragomiretskiy and Dominique Zosso. “Variational Mode Decomposition”. In: *IEEE Transactions on Signal Processing* 62.3 (2014), pp. 531–544. DOI: 10.1109/TSP.2013.2288675.
- [14] Geoffrey Fairchild et al. “Epidemiological Data Challenges: Planning for a More Robust Future Through Data Standards”. In: *Frontiers in Public Health* 6 (2018), p. 336. DOI: 10.3389/fpubh.2018.00336.
- [15] Xiaozi Gao et al. “Short-term wind power forecasting based on SSA-VMD-LSTM”. In: *Energy Reports* 9 (2023). 2022 The 3rd International Conference on Power and Electrical Engineering, pp. 335–344. ISSN: 2352-4847. DOI: <https://doi.org/10.1016/j.egyr.2023.05.181>. URL: <https://www.sciencedirect.com/science/article/pii/S2352484723009368>.
- [16] Herbert W. Hethcote. “The Mathematics of Infectious Diseases”. In: *SIAM Review* 42.4 (2000), pp. 599–653.
- [17] Sepp Hochreiter and Jürgen Schmidhuber. “Long short-term memory”. In: *Neural Computation* 9.8 (1997), pp. 1735–1780.
- [18] Songtao Huang et al. “TimeKAN: KAN-based Frequency Decomposition Learning Architecture for Long-term Time Series Forecasting”. In: *The Thirteenth International Conference on Learning Representations*. 2025. URL: <https://openreview.net/forum?id=wTLC79YNbh>.
- [19] Joshua P. Keller et al. “Tracking the transmission dynamics of COVID-19 with a time-varying coefficient state-space model”. In: *Statistics in Medicine* 41.15 (2022), pp. 2745–2767. DOI: <https://doi.org/10.1002/sim.9382>. eprint: <https://onlinelibrary.wiley.com/doi/pdf/10.1002/sim.9382>. URL: <https://onlinelibrary.wiley.com/doi/abs/10.1002/sim.9382>.
- [20] Patrick Kidger et al. “Neural Controlled Differential Equations for Irregular Time Series”. In: *Advances in Neural Information Processing Systems*. Ed. by H. Larochelle et al. Vol. 33. Curran Associates, Inc., 2020, pp. 6696–6707. URL: [https://proceedings.neurips.cc/paper\\_files/paper/2020/file/4a5876b450b45371f6cfe5047ac8cd45-Paper.pdf](https://proceedings.neurips.cc/paper_files/paper/2020/file/4a5876b450b45371f6cfe5047ac8cd45-Paper.pdf).
- [21] Benjamin C. Koenig, Suyong Kim, and Sili Deng. “KAN-ODEs: Kolmogorov–Arnold network ordinary differential equations for learning dynamical systems and hidden physics”. In: *Computer Methods in Applied Mechanics and Engineering* 432 (2024), p. 117397. ISSN: 0045-7825. DOI: <https://doi.org/10.1016/j.cma.2024.117397>. URL: <https://www.sciencedirect.com/science/article/pii/S0045782524006522>.

[22] Shiyang Li, Xiaoyong Jin, Yao Xuan, et al. “Enhancing the locality and breaking the memory bottleneck of transformer on time series forecasting”. In: *NeurIPS* (2019).

[23] Gabriel Michau, Gaetan Frusque, and Olga Fink. “Fully learnable deep wavelet transform for unsupervised monitoring of high-frequency time series”. In: *Proceedings of the National Academy of Sciences* 119.8 (2022), e2106598119. DOI: 10.1073/pnas.2106598119. eprint: <https://www.pnas.org/doi/pdf/10.1073/pnas.2106598119>. URL: <https://www.pnas.org/doi/abs/10.1073/pnas.2106598119>.

[24] Zuokun Ouyang, Philippe Ravier, and Meryem Jabloun. “STL Decomposition of Time Series Can Benefit Forecasting Done by Statistical Methods but Not by Machine Learning Ones”. In: *Engineering Proceedings* 5.1 (2021). ISSN: 2673-4591. DOI: 10.3390/engproc2021005042. URL: <https://www.mdpi.com/2673-4591/5/1/42>.

[25] M. Pivk and F.R. Le Diberder. “SPLOTS: A statistical tool to unfold data distributions”. In: *Nuclear Instruments and Methods in Physics Research Section A: Accelerators, Spectrometers, Detectors and Associated Equipment* 555.1 (2005), pp. 356–369. ISSN: 0168-9002. DOI: <https://doi.org/10.1016/j.nima.2005.08.106>. URL: <https://www.sciencedirect.com/science/article/pii/S0168900205018024>.

[26] Maziar Raissi, Paris Perdikaris, and George E. Karniadakis. “Physics-informed neural networks: A deep learning framework for solving forward and inverse problems”. In: *Journal of Computational Physics* 378 (2019), pp. 686–707.

[27] Carl Edward Rasmussen. “Gaussian Processes in Machine Learning”. In: *Advanced Lectures on Machine Learning: ML Summer Schools 2003, Canberra, Australia, February 2 - 14, 2003, Tübingen, Germany, August 4 - 16, 2003, Revised Lectures*. Ed. by Olivier Bousquet, Ulrike von Luxburg, and Gunnar Rätsch. Berlin, Heidelberg: Springer Berlin Heidelberg, 2004, pp. 63–71. ISBN: 978-3-540-28650-9. DOI: 10.1007/978-3-540-28650-9\_4. URL: [https://doi.org/10.1007/978-3-540-28650-9\\_4](https://doi.org/10.1007/978-3-540-28650-9_4).

[28] Alexander Rodríguez et al. “EINNs: epidemiologically-informed neural networks”. In: *Proceedings of the Thirty-Seventh AAAI Conference on Artificial Intelligence and Thirty-Fifth Conference on Innovative Applications of Artificial Intelligence and Thirteenth Symposium on Educational Advances in Artificial Intelligence. AAAI’23/IAAI’23/EAAI’23*. AAAI Press, 2023. ISBN: 978-1-57735-880-0. DOI: 10.1609/aaai.v37i12.26690. URL: <https://doi.org/10.1609/aaai.v37i12.26690>.

[29] Yulia Rubanova, Ricky T. Q. Chen, and David K Duvenaud. “Latent Ordinary Differential Equations for Irregularly-Sampled Time Series”. In: *Advances in Neural Information Processing Systems*. Ed. by H. Wallach et al. Vol. 32. Curran Associates, Inc., 2019. URL: [https://proceedings.neurips.cc/paper\\_files/paper/2019/file/42a6845a557bef704ad8ac9cb4461d43-Paper.pdf](https://proceedings.neurips.cc/paper_files/paper/2019/file/42a6845a557bef704ad8ac9cb4461d43-Paper.pdf).

[30] Sukhyun Ryu et al. “Epidemiology and Transmission Dynamics of Infectious Diseases and Control Measures”. In: *Viruses* 14.11 (Nov. 2022), p. 2510. DOI: 10.3390/v14112510.

[31] Jeffrey Shaman and Alicia Karspeck. “Forecasting seasonal outbreaks of influenza”. In: *Proceedings of the National Academy of Sciences of the United States of America* 109.50 (Dec. 2012), pp. 20425–20430. ISSN: 0027-8424. DOI: 10.1073/pnas.1208772109.

[32] Aleksei Sholokhov et al. “Physics-informed neural ODE (PINODE): embedding physics into models using collocation points”. In: *Scientific Reports* 13.1 (2023), p. 10166. ISSN: 2045-2322. DOI: 10.1038/s41598-023-36799-6. URL: <https://doi.org/10.1038/s41598-023-36799-6>.

[33] Naoya Takeishi, Yoshinobu Kawahara, and Takehisa Yairi. “Learning Koopman invariant subspaces for dynamic mode decomposition”. In: *Proceedings of the 31st International Conference on Neural Information Processing Systems. NIPS’17*. Long Beach, California, USA: Curran Associates Inc., 2017, pp. 1130–1140. ISBN: 9781510860964.

[34] Guancheng Wan et al. “EARTH: Epidemiology-Aware Neural ODE with Continuous Disease Transmission Graph”. In: *Forty-second International Conference on Machine Learning*. 2025. URL: <https://openreview.net/forum?id=Cnfgmxymj>.

[35] Shiyu Wang et al. “TimeMixer++: A General Time Series Pattern Machine for Universal Predictive Analysis”. In: *The Thirteenth International Conference on Learning Representations*. 2025. URL: <https://openreview.net/forum?id=1CLzLXSFNn>.

[36] Xiyuan Zhang et al. *First De-Trend then Attend: Rethinking Attention for Time-Series Forecasting*. 2022. arXiv: 2212.08151 [cs.LG]. URL: <https://arxiv.org/abs/2212.08151>.

[37] Haoyi Zhou et al. “Informer: Beyond efficient transformer for long sequence time-series forecasting”. In: *AAAI* (2021).

## A Failure Modes

We describe some of the architectures used for the experiments described in the Failure Modes section.

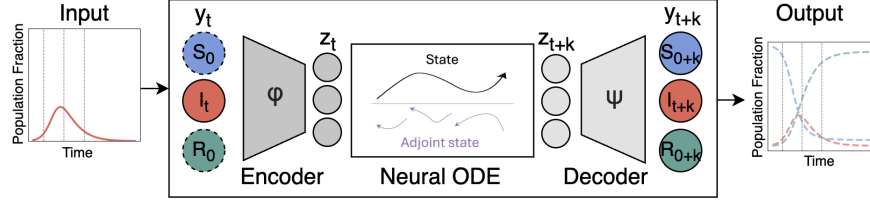


Figure A1: Overview of bidirectional AE-NODE framework.

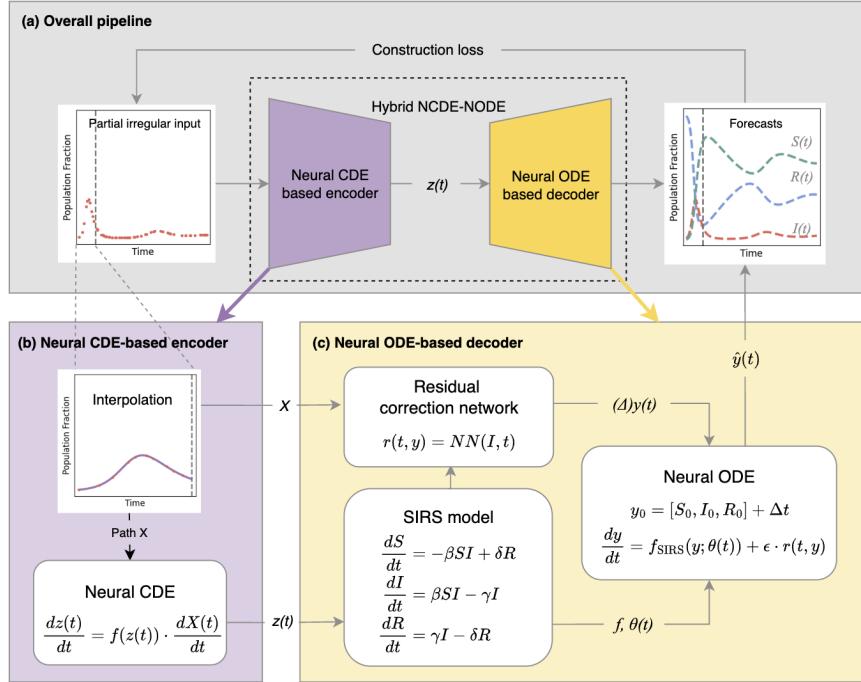


Figure A2: Overview of Neural CDE-ODE pipeline.

## B Training and Inference Procedure

Algorithm 1 summarizes the end-to-end training and inference procedure for EpiNode. Given a partially observed infection time series, the algorithm first performs trend–season–residuals decomposition to extract multi-scale control signals, which optionally undergo time-delay embedding. These controls drive a set of latent continuous-time Neural ODEs whose states are fused to infer time-varying epidemiological parameters. The inferred parameters are then used to advance the mechanistic SIRS model via numerical integration, producing epidemic state forecasts. Model parameters are optimized by minimizing the prediction error on observed infections over the training window, with gradients propagated through both the Neural ODE solvers and the mechanistic dynamics. At inference time, the learned model is rolled out beyond the observation window to generate long-horizon forecasts, peak estimates, and interpretable parameter trajectories.

## C Benchmarking Models

**Classical Statistical Baseline.** Autoregressive integrated moving-average (ARIMA) models serve as a classical statistical baseline for epidemic forecasting. ARIMA captures linear temporal dependencies through autoregressive and moving-average components and is commonly used for short-term epidemic prediction under near-stationary conditions.

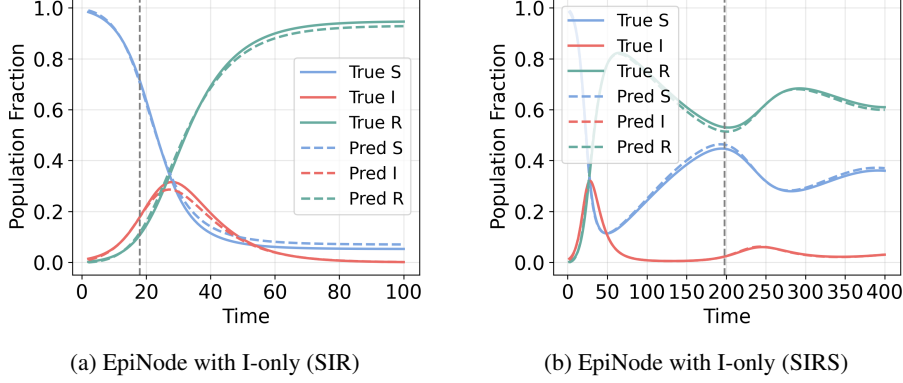


Figure A3: Success of forecasts from EpiNode under partial observability (I-only supervision) for (a) SIR and (b) SIRS.

**Algorithm 1** EpiNode training and forecasting

---

**Require:** Observations  $\{(t_i, I_i)\}_{i=0}^{T-1}$ , split index  $t_{\text{split}}$ , delay params  $(m, \tau)$ , step sizes  $\Delta t_i = t_{i+1} - t_i$   
**Require:** Model components: VMD; collaborated ODE fields  $f_{\theta_c}$ ; fusion MLP; parameter decoder  $g_\phi$ ; SIRS solver  
**Ensure:** Forecasted states  $\{\hat{y}(t_i)\}_{i=0}^{T-1}$  and parameters  $\{\beta(t_i), \gamma(t_i), \delta(t_i)\}_{i=0}^{T-1}$

- 1:  **$I(t)$  decomposition:**  $\{T_i, S_i, R_i\}_{i=0}^{T-1} \leftarrow \text{VMDDecompose}(\{I_i\})$  (8)
- 2: **Time delay construction:** build  $\mathbf{u}_i^{(T)}, \mathbf{u}_i^{(S)}, \mathbf{u}_i^{(R)}$  via delay embedding (9)
- 3: **Initialize state:**  $\hat{y}(t_0) = [1 - I_0, I_0, 0]^\top$  (1),(2)
- 4: **Initialize latents:**  $\mathbf{h}^{(T)}(t_0) = 0, \mathbf{h}^{(S)}(t_0) = 0, \mathbf{h}^{(R)}(t_0) = 0$  (10)
- 5: **for** epoch = 1 to  $E$  **do**
- 6:   Set loss  $\mathcal{L} \leftarrow 0$
- 7:   **for**  $i = 0$  to  $T - 1$  **do**
- 8:     **if**  $i > 0$  **then**
- 9:       **Latent ODE update (trend):**  $\mathbf{h}^{(T)}(t_i) \leftarrow \text{ODEINT}(f_{\theta_T}, \mathbf{h}^{(T)}(t_{i-1}), [t_{i-1}, t_i]; \mathbf{u}_{i-1}^{(T)})$  (11)
- 10:       **Latent ODE update (seasonal):**  $\mathbf{h}^{(S)}(t_i) \leftarrow \text{ODEINT}(f_{\theta_S}, \mathbf{h}^{(S)}(t_{i-1}), [t_{i-1}, t_i]; \mathbf{u}_{i-1}^{(S)})$  (11)
- 11:       **Latent ODE update (residual):**  $\mathbf{h}^{(R)}(t_i) \leftarrow \text{ODEINT}(f_{\theta_R}, \mathbf{h}^{(R)}(t_{i-1}), [t_{i-1}, t_i]; \mathbf{u}_{i-1}^{(R)})$  (11)
- 12:       **end if**
- 13:       **Fuse latents:**  $\mathbf{h}(t_i) \leftarrow \text{Fuse}([\mathbf{h}^{(T)}(t_i); \mathbf{h}^{(S)}(t_i); \mathbf{h}^{(R)}(t_i)])$  (12)
- 14:       **Decode rates:**  $(\tilde{\beta}, \tilde{\gamma}, \tilde{\delta}) \leftarrow g_\phi(\mathbf{h}(t_i))$  (13)
- 15:       **Affine scaling:**  $\beta(t_i), \gamma(t_i), \delta(t_i) \leftarrow \text{Scale}(\tilde{\beta}, \tilde{\gamma}, \tilde{\delta})$  (14)
- 16:       **Physics rollout:**  $\hat{y}(t_{i+1}) \leftarrow \text{RK4Step}(\hat{y}(t_i), \beta(t_i), \gamma(t_i), \delta(t_i), \Delta t_i)$  (15)
- 17:       **Mass correction:** apply simplex stabilization (16)
- 18:       **if**  $i < t_{\text{split}}$  **then**
- 19:         **Training loss:**  $\mathcal{L} \leftarrow \mathcal{L} + w_i(\hat{I}(t_i) - I_i)^2$  (17)
- 20:       **end if**
- 21:     **end for**
- 22:     **Normalize loss:**  $\mathcal{L} \leftarrow \mathcal{L} / t_{\text{split}}$  (17)
- 23:     **Parameter update:** backpropagate through ODE solvers to update  $\{f_{\theta_c}\}_{c \in \{T, S, R\}}$ , Fuse, and  $g_\phi$
- 24:   **end for**
- 25: **return**  $\{\hat{y}(t_i)\}_{i=0}^{T-1}$  and  $\{\beta(t_i), \gamma(t_i), \delta(t_i)\}_{i=0}^{T-1}$

---

**Recurrent Neural Network Baseline.** We include standard recurrent neural networks (RNN) and gated variants (LSTM/GRU) as nonlinear sequence modeling baselines. RNN-based models can capture complex temporal dependencies from data but operate as black-box predictors and do not enforce epidemiological constraints.

**Time–Frequency–Based Univariate Forecasting Methods.** TimeKAN [18] and TimeMixer++ [35] represent recent state-of-the-art univariate forecasting models that leverage decomposition or multiscale mixing to capture long-range temporal patterns, providing strong data-driven baselines.

**Physics-Informed Neural Model.** To incorporate epidemiological structure, we include EINN [28], a physics-informed neural model that embeds epidemic priors into neural forecasting without explicit continuous-time latent dynamics. As EINN employs SEIRm physics, we adapt the framework in two ways: (1) replacing SEIRm with SIRS and (2) predicting  $I$  rather than  $m$ . In both cases,  $I$  is the only observed compartment.

**Continuous-Time Neural ODE Models.** We further evaluate ODE-based continuous-time models, including Neural ODE [9], Latent ODE [29], and KAN-ODE [21], which model temporal evolution via learned differential equations but do not enforce epidemic physics by default.

**Graph-Based Neural ODE Model.** Finally, we consider EARTH [34], a graph-based neural ODE model that integrates epidemiological dynamics with spatial coupling. Since we focus on single-region forecasting, we treat the region as a graph with  $N = 1$  node and set the adjacency matrix to  $A = [1]$ .

## D Signal Decomposition Methods

We compare several signal decomposition techniques that differ in their assumptions about temporal structure, frequency separation, and modeling capacity. Each method decomposes the observed infection time series into components that are subsequently used to control latent continuous-time dynamics.

**Variational Mode Decomposition (VMD).** VMD decomposes a signal into a predefined number of intrinsic mode functions, each constrained to be band-limited around a learned center frequency [13]. The decomposition is obtained by solving a variational optimization problem in the frequency domain that jointly minimizes bandwidth and reconstruction error. VMD produces components with well-separated frequency content and is robust to noise, making it well suited for isolating multi-scale epidemic dynamics.

**Moving Average (MA).** The moving average (MA) decomposition applies a sliding-window average to smooth short-term fluctuations and extract a low-frequency trend component [36]. Residuals are obtained by subtracting the smoothed signal from the original series. MA provides a simple baseline that captures coarse trends but does not explicitly model seasonality or frequency structure, and is sensitive to window size selection.

**Seasonal–Trend Decomposition using Loess (STL).** STL decomposes a time series into additive trend, seasonal, and residual components using locally weighted regression (LOESS) [24]. It assumes a fixed seasonal period and smooth temporal evolution, making it effective for stationary or weakly nonstationary seasonal patterns. However, STL does not enforce explicit frequency separation and may struggle when seasonal dynamics vary over time or across epidemic waves.

**Wavelet Decomposition.** Wavelet-based decomposition represents the signal using a set of scaled and shifted wavelet basis functions, yielding a multi-resolution time–frequency representation [23]. This approach captures both local temporal variations and global structure. While wavelets provide strong localization in time and frequency, the resulting components are not necessarily narrowband, and performance depends on the choice of wavelet family and decomposition depth.

**SSA–VMD (Hybrid Decomposition).** SSA–VMD combines Singular Spectrum Analysis (SSA) with VMD to leverage the strengths of both methods [15]. SSA first separates the signal into dominant subspaces corresponding to trend and oscillatory modes using low-rank trajectory matrices. VMD is then applied to selected components to further refine frequency separation. This hybrid approach improves robustness in noisy settings but introduces additional complexity and hyperparameters.

**Neural Koopman Decomposition.** Neural Koopman methods learn a latent linear dynamical system by lifting the observed time series into a higher-dimensional feature space using neural networks [33]. Decomposition is achieved by projecting dynamics onto learned Koopman modes and eigenfunctions. This approach is fully data-driven and expressive, but does not explicitly enforce band-limited or frequency-localized components, which can lead to entangled modes under strong nonstationarity.

## E Dataset Details

To comprehensively evaluate epidemic forecasting performance under partial observability, time-varying dynamics, and physics mismatch, we benchmark our approach on a diverse suite of synthetic and real-world datasets, spanning multiple disease regimes, observation settings, and experimental conditions.

### E.1 Synthetic Datasets

**SIRS with Time-Fixed and Time-Varying Parameters.** We generate synthetic epidemics using the SIRS model under multiple parameter regimes. In the fixed setting, transmission, recovery, and immunity-loss rates remain constant over time, serving as a baseline for identifiability under stationarity. In the periodic setting, parameters vary smoothly and periodically to emulate seasonal forcing, capturing recurring epidemic patterns.

**Different Epidemic Physics.** To assess robustness to physics mismatch, we additionally simulate data from alternative compartmental models. The SIR setting removes immunity waning, testing the model’s ability to adapt when the assumed SIRS structure is overparameterized. The SEIRS setting introduces an exposed compartment, increasing latent-state complexity and evaluating performance when the true dynamics deviate from the assumed model class.

### E.2 Real-World Datasets

We evaluate on multiple real-world epidemic datasets that exhibit both seasonal and non-seasonal dynamics.

**Seasonal Epidemics.** Influenza-like illness (ILI) surveillance data (<https://gis.cdc.gov/grasp/fluvview/fluportaldashboard.html>) provides a canonical example of strongly seasonal epidemic dynamics. We consider two settings: single-wave segments, obtained by isolating individual seasonal outbreaks, and multi-wave sequences spanning multiple years. This allows evaluation of both early outbreak forecasting and long-term seasonal recurrence. We evaluate across multiple U.S. Department of Health and Human Services (HHS) regions and time periods, capturing heterogeneity in epidemic progression and reporting practices.

**Non-Seasonal Epidemics.** To assess generalization beyond seasonal diseases, we additionally evaluate on a non-seasonal dataset of COVID-like illness symptoms (CLS) provided by Delphi/COVIDcast (<https://delphi.cmu.edu/covidcast/survey-results/?date=20220625>). We use the 7-day averaged CLS signal for the United States, spanning April 15, 2020 to June 25, 2022, and focus on the first epidemic wave to isolate non-seasonal dynamics. This dataset consists of symptom-based surveillance measurements with irregular, non-periodic behavior, providing a complementary testbed for evaluating model robustness beyond seasonal epidemic settings.

## F Implementation via Bounded Parameterization.

Rather than fixing parameters or imposing strong smoothness priors, we implement these ranges through a bounded neural parameterization, where raw network outputs are mapped via a sigmoid function and affine scaling into the prescribed intervals. This approach follows prior work on constrained neural modeling of dynamical systems and epidemic processes [26, 10]. By encoding epidemiological knowledge as soft constraints, the model remains expressive while producing parameter trajectories that are interpretable, numerically stable, and consistent with known disease characteristics.

## G Supplementary Results

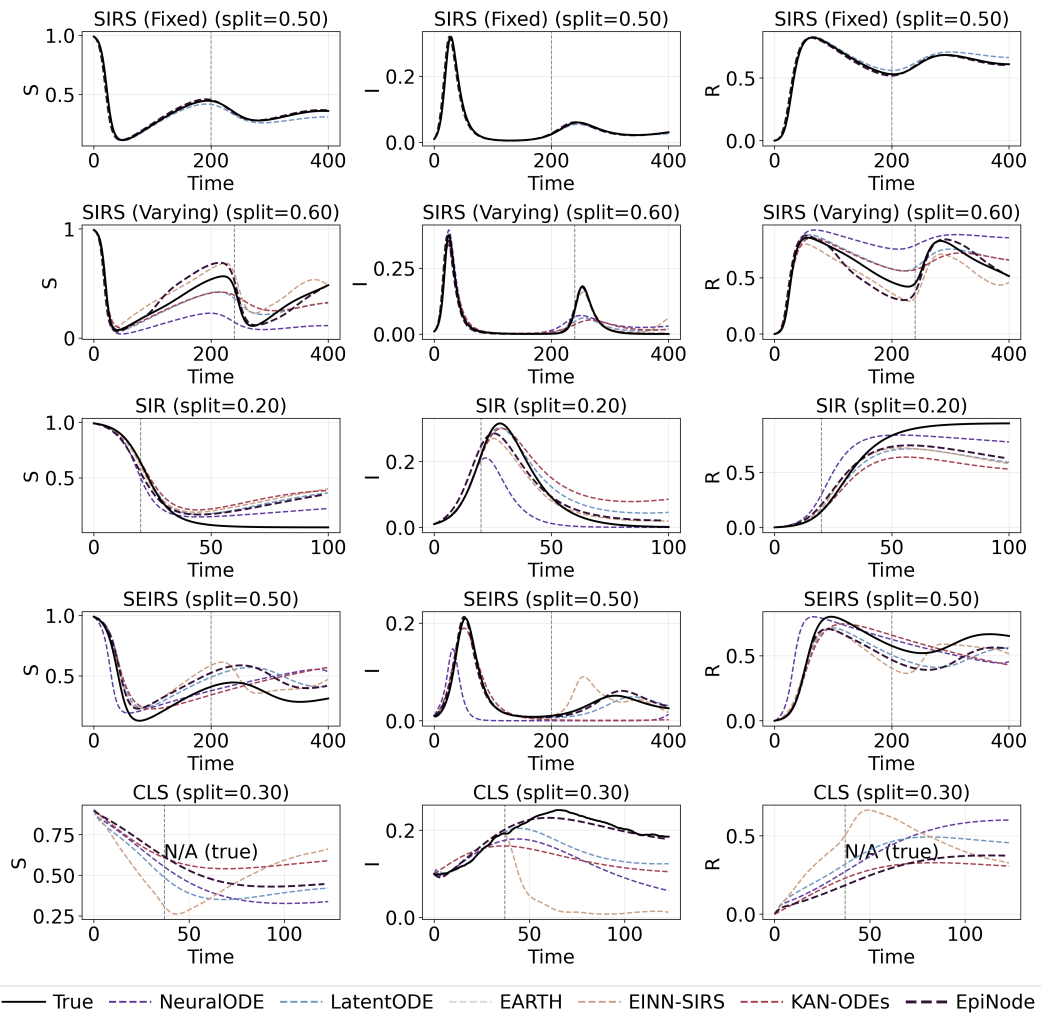


Figure A4: True and predicted compartments for synthetic datasets.

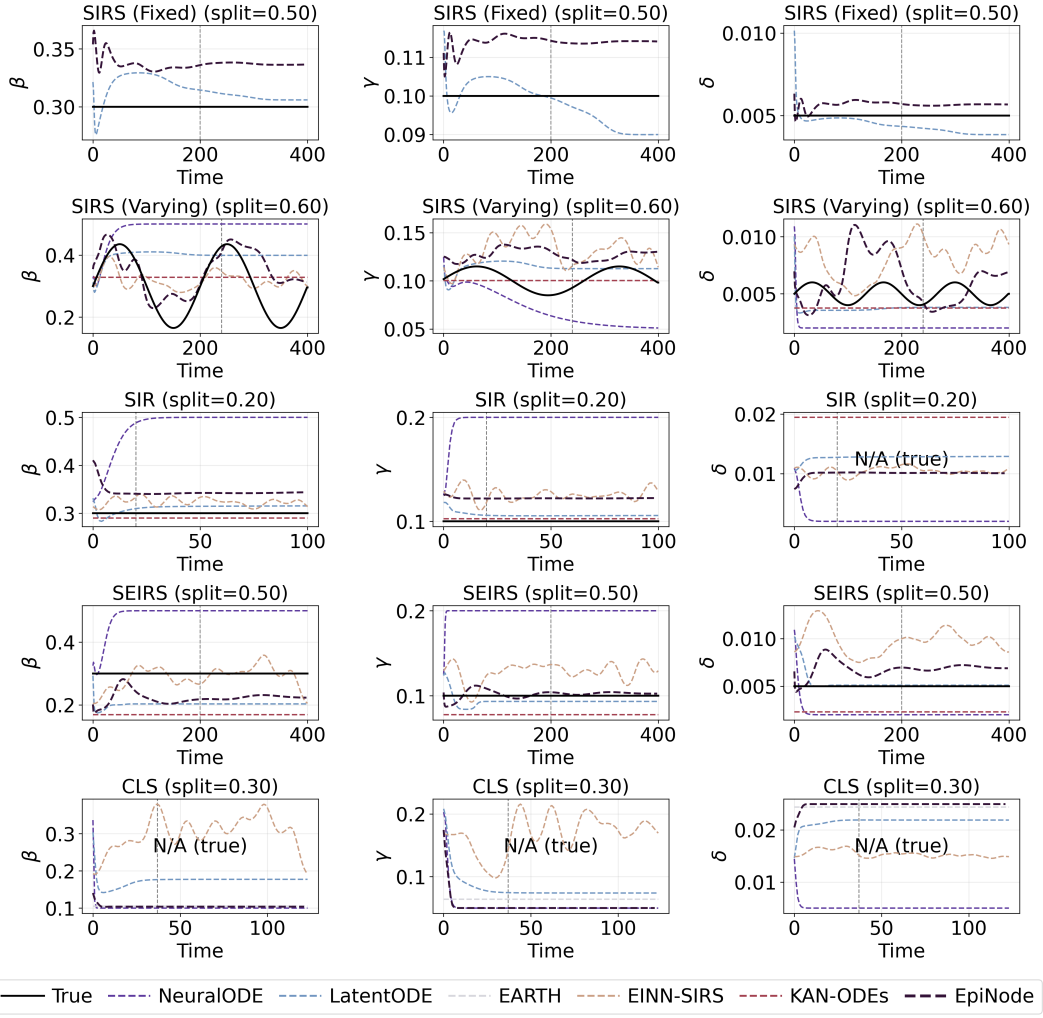


Figure A5: True and predicted parameters for synthetic datasets.)

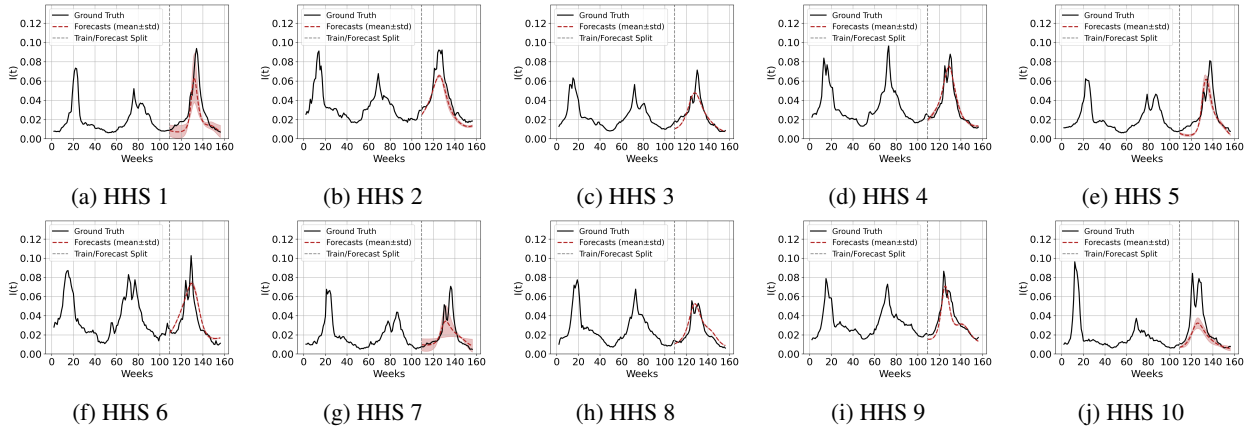


Figure A6: Forecasts across all HHS regions at split 0.7.